CONDENSED MATTER PHYSICS

Scaling, rotation, and channeling behavior of helical and skyrmion spin textures in thin films of Te-doped Cu_2OSeO_3

M.-G. Han[1]*†, J. A. Garlow[1†], Y. Kharkov[2†], L. Camacho[3], R. Rov[3,4], J. Sauceda[2], G. Vats[5], K. Kisslinger[6], T. Kato[7], O. Sushkov[2], Y. Zhu[1]*, C. Ulrich[2], T. Söhnel[3,4]*, J. Seidel[5]*

Topologically nontrivial spin textures such as vortices, skyrmions, and monopoles are promising candidates as information carriers for future quantum information science. Their controlled manipulation including creation and annihilation remains an important challenge toward practical applications and further exploration of their emergent phenomena. Here, we report controlled evolution of the helical and skyrmion phases in thin films of multiferroic Te-doped Cu_2OSeO_3 as a function of material thickness, dopant, temperature, and magnetic field using in situ Lorentz phase microscopy. We report two previously unknown phenomena in chiral spin textures in multiferroic Cu_2OSeO_3: anisotropic scaling and channeling with a fixed-Q state. The skyrmion channeling effectively suppresses the recently reported second skyrmion phase formation at low temperature. Our study provides a viable way toward controlled manipulation of skyrmion lattices, envisaging chirality-controlled skyrmion flow circuits and enabling precise measurement of emergent electromagnetic induction and topological Hall effects in skyrmion lattices.

INTRODUCTION

Skyrmions, i.e., smooth and topologically stable spin textures with a nontrivial topology (*1*, *2*), potentially offer notable advancement for the regime of next-generation electronics (*3*, *4*), spintronics (*5*), and condensed matter physics (*6*–*10*). Magnetic skyrmions have been reported in several chiral magnetic single crystals (*11*–*13*), polycrystalline alloys (*14*), multilayered thin films (*15*–*18*), and multiferroics (*19*, *20*) and are envisaged as potential candidates for high-density racetrack memories (*21*), cache memory (*22*), ultralow energy spintronic switches (*23*), and skyrmion reshufflers for probabilistic computing (*24*). For the realization of these potential applications, the energy efficient creation, annihilation, and controlled manipulation of skyrmion lattices (SkLs) (*5*, *25*, *26*) in designed architectures are essential. Manipulation of SkLs has been demonstrated using spin-polarized currents (*27*), electric field (*28*), uniaxial strains (*29*), boundary conditions (*30*, *31*), and magnetoelectric coupling (*32*–*34*). However, deterministic control of SkLs still remains elusive, thus necessitating systematic studies for tailored boundary conditions.

Insulating Cu_2OSeO_3 (CSO) has gained notable interest due to its magnetoelectric coupling and is considered as an ideal platform to achieve electric field control of SkLs. Recently, an intriguing discovery of a new skyrmion phase (*35*) and of low-temperature skyrmions (*36*, *37*) has been made in CSO crystals, implying richer phase diagrams. The existence of two distinct skyrmion phases in a multiferroic material could be a generic character of underlying physics and may assist in skyrmion manipulation (*36*). In chiral cubic CSO crystals, the structure and prevalence of the spin textures are determined by the competing magnetic Hamiltonian terms: exchange correlation (J), relativistic Dzyaloshinskii-Moriya (DM) interactions, and crystal anisotropy energy. The magnetic ground state in CSO crystals at low temperature is represented by helical spin arrangements with the modulation period (λ) proportional to the ratio of J and DM interactions (*15*). Within a range of an applied external magnetic field, a hexagonally packed SkL along the direction of the applied magnetic field is predictably formed.

Chemical doping has been used to enhance DM interactions in B20 compounds due to the resulting variation in DM vector or electronic band filling (*38*). Similarly, it has been shown that the energy bandgap values change with the Te-dopant concentration in CSO crystals that affects the magnetic properties of the system (*39*). For one-dimensional (1D) or 2D confined structures, helical spin textures are often observed to be distorted, and geometric anisotropies develop because of important roles played by surface/interface and demagnetization (or stray field) effects. In general, the skyrmion phase can be stabilized over wider ranges of temperature (T) and magnetic field (H) in confined structures, compared to the narrow A-phase in bulk crystals. Thus, a systematic study on chemical doping and sample geometry is necessary to understand the skyrmion phase dynamics in multiferroic CSO crystals toward their deterministic manipulation.

Here, we report the study of systematic control of helical-to-skyrmion phase transitions in thin films of multiferroic Te-doped CSO single-crystals as a function of material thickness, doping, temperature, and magnetic field. By in situ Lorentz phase microscopy, nanoscale magnetic spin evolutions in tailored thin films were directly imaged to obtain Te-doping and thickness-dependent phase maps obtained over a range of T and H. With increasing magnetic field, we find an anisotropic nonlinear change in the spiral helix periodicity accompanied by reduced Lorentz imaging contrast that are associated with out-of-plane tilting of the helix based on our theoretical model. In addition, we report gradual skyrmion injection from thinner to thicker sections with an edge-locked wave vector,

[1]Condensed Matter Physics and Materials Sciences Department, Brookhaven National Laboratory, Upton, NY 11973, USA. [2]School of Physics, UNSW Sydney, Sydney, NSW 2052, Australia. [3]School of Chemical Sciences, University of Auckland, Auckland 1142, New Zealand. [4]MacDiarmid Institute of Advanced Materials and Nanotechnology, Victoria University of Wellington, Wellington, New Zealand. [5]School of Materials Science and Engineering, UNSW Sydney, Sydney, NSW 2052, Australia. [6]Center for Functional Nanomaterials, Brookhaven National Laboratory, Upton, NY 11973, USA. [7]Nanostructures Research Laboratory, Japan Fine Ceramics Center, Nagoya, Japan. *Corresponding author. Email: mghan@bnl.gov (M.-G.H.); zhu@bnl.gov (Y.Z.); t.soehnel@auckland.ac.nz (T.S.); jan.seidel@unsw.edu.au (J.Se.)
†These authors contributed equally to this work.

termed "skyrmion channeling." Our systematic study demonstrates that thickness and Te doping are viable parameters for controlling skyrmion *H*-*T* phase spaces in multiferroic CSO. The thickness-dependent skyrmion channeling envisages chirality-controlled skyrmion injections in skyrmion flow circuits for designing future skyrmionic devices.

RESULTS AND DISCUSSION

Lorentz phase images (Fig. 1, B and C) taken at 25 K and under a small residual magnetic field (~11.7 mT) show two helical spin modulations ($h_{[110]}$ and $h_{[001]}$) with wave vectors *Q* oriented along [110] and [001] directions, respectively. The $h_{[110]}$ is observed in the area near the original surface, while the $h_{[001]}$ modulation is found in the area far from the Pt/CSO surface in both samples. Using the transport-intensity-equation–based phase-retrieval method (*40*), we reconstructed the magnetic induction map of helical phases for both samples, as shown in Fig. 1 (D and E). The modulation periods (λ) at 11.7 mT measured from the magnetic induction map were 58 and 61 nm for the undoped and doped samples, respectively, implying that Te-doping effects result in a slight change in the ratio between J and DM interactions. Shibata *et al.* (*41*) extensively studied the doping effect in $Mn_{1-x}Fe_xGe$ and found a marked impact on skyrmion size depending on crystal composition and point to competing interactions such as magnetic anisotropy and exchange interactions for the compensation of a weakened DM interaction. In our study, the DM interaction becomes weakened by the Te substitution with respect to the exchange interaction J due to the increase in the lattice constant by substitutional Te doping (ionic radius of Te^{4+} is larger than that of Se^{4+} by ~10%). However, the exact impact of doping on the nature of DMI and other relevant energies in CSO requires further theoretical investigation. At the applied field of 82.6 mT, both samples showed SkLs with lattice constants of 67 and 72 nm, respectively (Fig. 1, F and G). Eventually, the SKLs destabilize and reach the poled ferromagnetic state at large magnetic fields.

The magnetic-field dependence of the spin textures at 25 K is shown in Fig. 2 (a series of Lorentz images obtained with the increase of applied magnetic field perpendicular to the sample). Corresponding diffractograms from each thickness section show that the evolution of helical-skyrmion phases is clearly thickness dependent. The $h_{[110]}$ phase shows a notable expansion in its modulation period and a clockwise rotation up to ~15° with increasing magnetic field (for example, compare $h_{[110]}$ between 11.7 and 62 mT in the t = 100 nm section).

In contrast, the modulation period of the $h_{[001]}$ phase does not change notably, while its area gradually decreases with increasing magnetic field. In neutron scattering experiments, the helical states at low magnetic fields are observed along the cubic axes in CSO due to the cubic magnetic anisotropy. We note that the $h_{[110]}$ phase deviates from the cubic axis and only shows a scaling behavior with applied magnetic field. We discuss this anisotropic scaling behavior of helical phases later in more detail.

At the applied field of 41.5 mT, skyrmions begin to nucleate at the edge of the thinnest section (t = 69 nm), as shown in Fig. 2B. Similar nucleation at the sample edge has been reported in metallic FeGe crystals and attributed to preferential nucleation at distorted edge states in the helix (*42*). Two sets of SkLs (SkL_1 and SkL_2) are initially formed independently (see the t = 69 nm section with 62 mT and its Fourier transform in Fig. 2C), of which wave vectors are tilted 30° away from each other. With increasing magnetic field, SkL_1 becomes dominant over the other, eventually the sample is encompassed by a single set of SkL_1. The evolution of magnetic spin textures in the Te-doped and undoped CSO samples at 25 K shows sequential "skyrmion filling" from thinnest sections to thicker ones with increasing magnetic field from 11.7 to 184.3 mT (see the Supplementary Materials for data of helical-skyrmion phase dynamics for the undoped sample). With further increase in magnetic field, the SkL destabilizes and rotates locally that indicates the wave vector coherence has been lost between neighboring sections as demonstrated by the presence of Moiré fringes in the t = 100 nm section at 163.8 mT. Subsequently, SkLs expand with increased

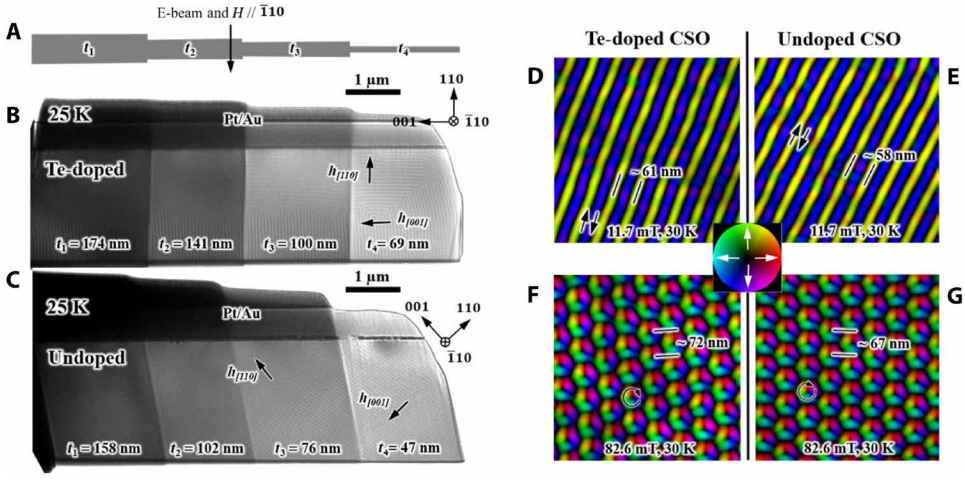

Fig. 1. Real-space observation of magnetic spin textures in Te-doped and undoped CSO thin films. (**A** to **C**) Sample schematic and Lorentz images of Te-doped and undoped CSO transmission electron microscopy samples at 25 K under residual magnetic field (H ~ 11 mT) along the [$\bar{1}$10] direction. Four different thickness sections are prepared by focused ion beam for both undoped and doped samples. (**D** to **G**) Magnetic induction maps reconstructed by the phase retrieval method for doped (D) and (F) and undoped (E) and (G) samples, respectively, showing helical spin states (D) and (E) and hexagonally packed SkLs (F) and (G). Color wheel shown in the center represents amplitude and direction of magnetization.

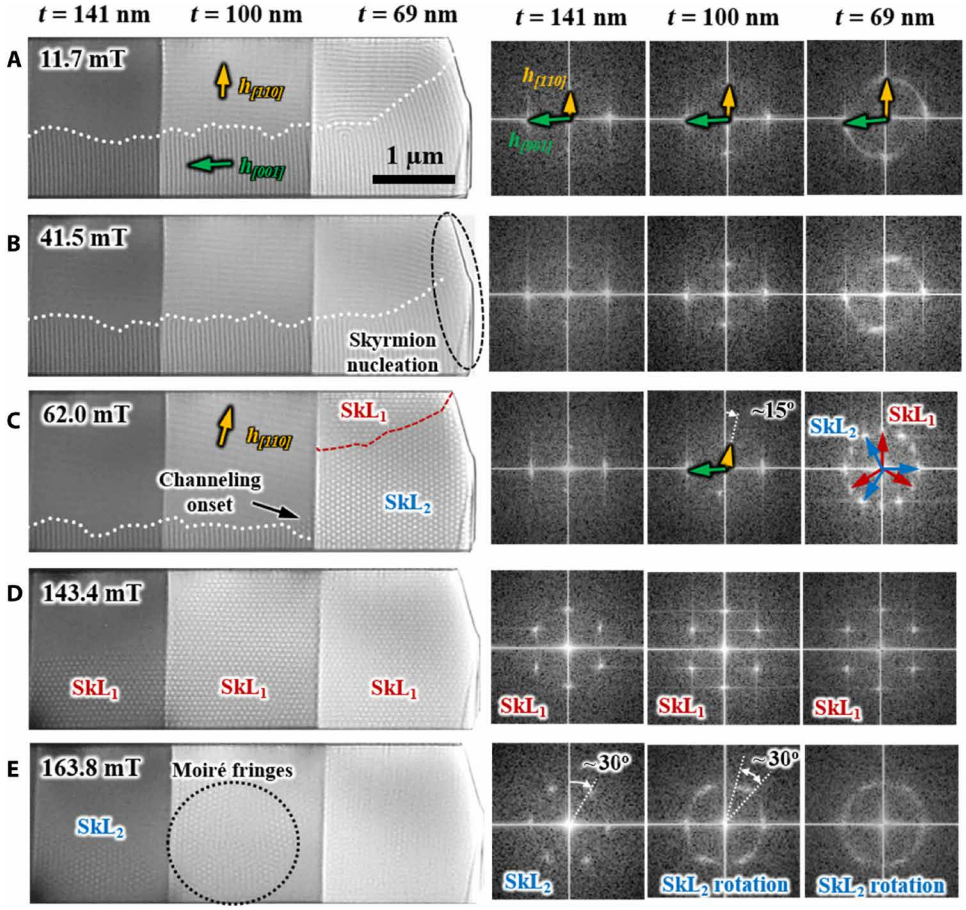

Fig. 2. Evolution of spin textures under various magnetic field. Helical-to-skyrmion phase transition in Te-doped CSO observed by Lorentz microscopy at 25 K under various external magnetic fields (*H*) along the [110] direction (**A** to **E**). Lorentz phase images from three different thicknesses (69, 100, and 141 nm, respectively) and their corresponding diffractograms (right) showing field and thickness dependence of the spin textures. Anisotropic scaling of two orthogonal helical phases, edge-induced skyrmion nucleation, and skyrmion channeling are observed upon magnetic field application.

rotation up to 30° clockwise before eventual transitioning to the uniform ferromagnetic phase.

The evolution of magnetic spin textures in both undoped and doped samples at 25 K shows sequential skyrmion channeling, in which the SkL nucleates from the helical phase at the edge of the thinnest sample section and propagates to the thicker section, through the helical phase, with increasing magnetic field (Fig. 1, B and C). We term skyrmion channeling as the sequential filling of different thickness sections with skyrmions through transformation of the $h_{[001]}$ helices. We demonstrate that the channeling process for both the doped and undoped samples at lower temperatures, where the helical-skyrmion phase dynamics are less affected by thermal fluctuations, proceeds rather slowly. Figure 3 shows Lorentz images from the two thinnest sections of the doped and undoped samples near the onset of channeling at 15 K. Two sets of SkLs (SkL_1 and SkL_2) are observed in both samples upon skyrmion nucleation. SkL_1 is bound to the top and bottom of the sample edges. Channeling occurs predominantly along the bottom edge into the thicker section [the top edge has Au/Pt from focused ion beam (FIB) preparation], as indicated with blue arrows in Fig. 3 (B and D). As channeling progresses, the SkL_1 expands at the expense of SkL_2 in both doped and undoped samples. This channeling process at 15 K occurs over a time of about 20 s, as shown in Fig. 3. Effects of geometric confinement and the presence of discrete boundaries have been studied theoretically and experimentally in other skyrmion systems (*43*–*45*). Our findings of skyrmion channeling and anisotropic scaling provide important insight toward skyrmion manipulation. Note that the channeling SkL (SkL_1) in both the doped and undoped samples have a wave vector component normal to the bottom sample edge. It should be noted that the bottom edge of the doped sample is along the cubic axes ([100]), but that of the undoped sample is 45° tilted from the cubic axes. Similar edge-locked skyrmion wave vectors are reported in FeGe nanostripes (*43*). We suggest that optimally packed skyrmions at the sample edge minimize fringing fields leading to formation of skyrmion chains along the edges with the wave vector along the normal to the edge. The Moiré fringes found in Fig. 2E occur when the edge-locked skyrmions are detached from the edges and thus are free to rotate. We note that edge geometries, specifically the presence of Au/Pt on one surface, may influence the evolution of skyrmion phases and is worth further investigation. Effects of different edge termination and local strains play important roles on phase transitions and spin texture evolution upon external magnetic field. These edge-locked SkL wave vectors, independent of doping, thickness, temperature, and underlying crystallographic directions, provide a viable way to realize skyrmion flow circuits in thin-film geometry for practical applications.

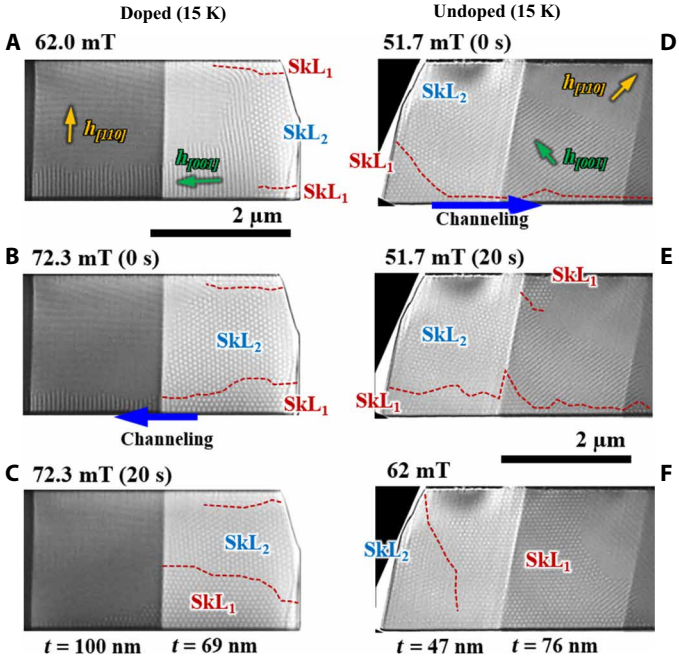

Fig. 3. Thickness controlled skyrmion "channeling." Skyrmions nucleated at edges in the thinnest section gradually channel across thicker sections. Both doped (**A** to **C**) and undoped (**D** to **F**) samples show skyrmion channeling. Red dashed lines separate SkL_1 and SkL_2.

The anisotropic scaling behaviors (dependency of the helical modulation period on external magnetic field) in the doped and undoped samples are plotted in Fig. 4. The $h_{[110]}$ phases (domain II) show a marked expansion of up to 35%, particularly in the t = 100 nm section. In contrast, the $h_{[001]}$ phase (domain I) expansion is notably less prominent and below 5%. Similar scaling behavior is observed in SkLs (initial lattice constant of ~70 nm under 11 mT to 130 nm under 200 mT, measured with diffractograms shown in Fig. 2). In addition to the wavelength expansion, the modulation amplitude of the spin spiral in the domain II drops compared to the domain I by a factor of ~5 to 10 with increasing magnetic field H. The observed effects of the helix modulation period expansion strongly depend on the thickness of the CSO film. These experimental observations can be naturally explained if we assume that, at finite magnetic field H, spin spiral in the domain II tilts out of plane toward the direction of the magnetic field, as shown Fig. 5A. The in-plane component of wave vector of the spiral tilted at the angle θ decreases as $Q_{||} = Q\cos(\theta)$; hence, the period of the spiral measured in Lorentz microscopy $\lambda = 2\pi/(Q\cos(\theta))$ increases with the tilting angle θ. A similar phenomenon of tilting of the spin spiral in CSO crystals toward the direction of the magnetic field was observed in bulk measurements with small-angle neutron scattering (*35*, *36*) and has been attributed to a competition between either cubic and exchange anisotropies (*35*) or cubic anisotropy and dipolar interactions (*36*).

From a theoretical point of view, we can understand this behavior as follows. The spin spiral in CSO crystals is generated by the DM interaction, the energy density reads

$$\varepsilon = \frac{\rho}{2}(\nabla \boldsymbol{m})^2 + D(\boldsymbol{m}\cdot[\nabla\times\boldsymbol{m}]) - (\boldsymbol{m}\cdot\boldsymbol{H}) \quad (1)$$

where ρ is the spin stiffness and $\boldsymbol{m}$ is the unit vector along the magnetization, $\boldsymbol{m}^2 = 1$. The DM interaction creates a proper screw spin helix with wave vector $|\boldsymbol{Q}| = D/J$, and the direction of the spin spiral in the bulk is arbitrary. Spiral tilting is caused by the interplay of magnetocrystalline anisotropy in CSO films as well as the interaction of the spin helix with the magnetic field. CSO has a cubic crystalline symmetry, intrinsic magnetic anisotropies favor the $\boldsymbol{Q}$ vector of the spiral to be oriented along principal crystal axes (*35*). The anisotropy energy of the spin helix in the lowest in Q approximation can be written in the form $\varepsilon^{(1)}_{\text{anis}} = -\frac{\kappa_{\text{eff}}}{2}\left(\widehat{\boldsymbol{Q}}_1^4 + \widehat{\boldsymbol{Q}}_2^4 + \widehat{\boldsymbol{Q}}_3^4\right)$, where $\widehat{\boldsymbol{Q}} = \boldsymbol{Q}/Q$ is the unit vector along $\boldsymbol{Q}$, and indexes 1, 2, and 3 correspond to the principal crystal directions. This is the only kinematic structure caused by fourth-rank tensor anisotropy terms allowed by crystal symmetries.

In very thin films, the energy of the out-of-plane spin spiral with $\widehat{Q}\|\hat{z}$ is higher compared to the energy of the spin spiral with $\widehat{Q}\perp\hat{z}$, where $\hat{z}$ is the unit vector orthogonal to the film surface. Two effects can change the energy of the out-of-plane spin spiral compared to the in-plane in thin films: (i) demagnetizing (stray) fields and (ii) easy-axis anisotropy $\varepsilon_{\text{axis}} \sim -\frac{\beta(t)}{2} m_z^2$, where $\beta(t)$ is a decreasing function of the film thickness t, $\beta(t) \propto 1/t$. The anisotropic contribution to the energy of the spiral due to the finite-thickness effects (i) and (ii) can be modeled as $\varepsilon^{(2)}_{\text{anis}} \approx \frac{\beta(t)}{2}\sin^2\theta$. The combination of the demagnetizing (stray) fields and the easy-axis anisotropy likely results in the unusual behavior of the spin helices in domains I and II.

At sufficiently small magnetic fields, the minimum energy in the domain I corresponds to θ = 0; see Fig. 4A. Therefore, the wave vector of the spin spiral is a constant as a function of the perpendicular magnetic field H. Conversely, for the domain II, the energy is minimal at a nonzero tilting angle θ(H) (see Fig. 4A), and the tilting angle evolves with the magnetic field. The corresponding theoretical curves for $\lambda(H) = \frac{\lambda_0}{\cos(\theta)}$ are shown with solid lines in Fig. 4 (B and C). Fitting experimental data for λ (H) in doped and undoped CSO films result in the following values of the phenomenological parameters: $k_{\text{eff}}/(\rho Q^2) \approx 0.5$ and $\beta/(\rho Q^2) \sim 0.1$ to 0.2; see Fig. 4D (see the Supplementary Materials for details). The absolute energy scale ρQ^2 can be approximately determined from the bulk phase diagram of CSO in the external magnetic field. The transition from the conical spiral phase to the field-polarized phase at low temperatures occurs at the critical magnetic field $H_{c2} = \rho Q^2/\mu \approx 100$ mT. The magnetic moment of Cu^{2+} per unit volume is $\mu \approx 0.44\mu_B n_{Cu} \approx 11\ \mu_B/\text{nm}^3$ [see (*41*)], where $n_{Cu} \approx 2.22 \times 10^{22}\ \text{cm}^{-3}$ is the number density of the Cu ions. Therefore, we obtain $\rho Q^2 \approx 60\ \mu\text{eV/nm}^3$. Independent measurements of spin wave transport in CSO can be used to extract the spin stiffness $\rho \sim 0.65 \times 10^{-4}\ \text{J/m}^3$ [see (*46*)], which gives $\rho Q^2 \approx 44\ \mu\text{eV/nm}^3$ in a good agreement with the previous estimate.

The out-of-plane tilting of the spiral results in the decrease of the relative ratio of helix amplitude A in domains II and I measured with Lorentz microscopy. Since Lorentz microscopy probes the averaged in-plane spin component over the thickness of the sample, we obtain the amplitude suppression

$$\langle\cos(Q_x x + Q_z z)\rangle = \int_0^t \frac{dz}{t}\cos(Q_x x + Q_z z) = A\cos(Q_x x + \phi(Q_z)),$$
$$\text{where } A = \frac{|\sin(Q\sin(\theta)\,t/2)|}{Q\sin(\theta)\,t/2} \quad (2)$$

The tilting angle $\theta = \arccos\left(\frac{\lambda_0}{\lambda(H)}\right)$ can be directly extracted from experimental data presented in Fig. 4 (B and C). The data show tilting

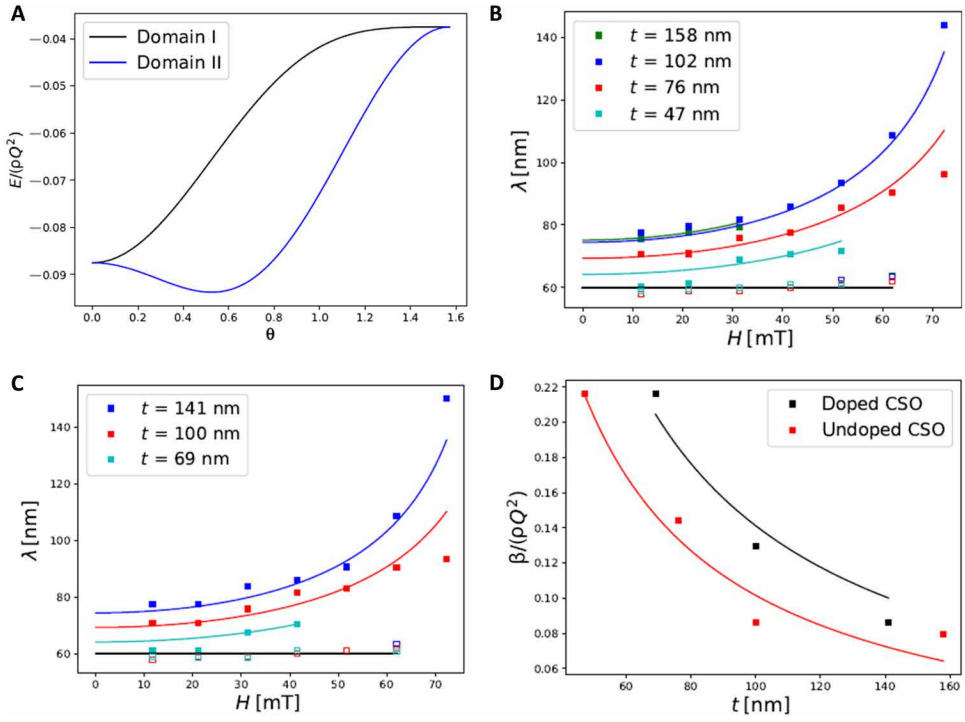

Fig. 4. Anisotropic scaling behavior of helical spin states. (**A**) Anisotropic contribution to the energy of the spin spiral in domains I and II at $H/(\rho Q^2) = 0.5$, $\beta/(\rho Q^2) = 0.1$, $k_{eff}/(\rho Q^2) = 0.5$. (**B** and **C**) Comparison of experimental data on the scaling of the measured spin spiral wave vector $Q_{||}$ versus perpendicular magnetic field H in (A) undoped CSO, (C) Te-doped CSO. Squares show experimental data, and blue, red, and cyan solid lines are the fit with the theoretical formula, eq. S7. The open (filled) markers correspond to spirals in domain I, the $h_{[001]}$ phase (domain II, the $h_{[110]}$ phases). The black solid line is the theoretical prediction for the domain I, $\lambda = \lambda_0$. (**D**) Extracted value of the phenomenological parameter β versus sample thickness t. The solid lines show $\beta(t) \propto 1/t$.

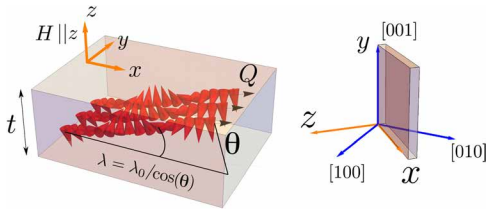

Fig. 5. Tilting of the helical propagation vector in finite field. Left: Out-of-plane tilting of the spin *h[110]* spiral in the external magnetic field (domain II) $H||z$. Right: Orientation of the crystal axes in the CSO sample.

angles of the spiral in domain II in the range of θ ~ 20° to 65°. Taking the values of the angle θ from the data, we estimate a Lorentz microscopy amplitude suppression factor A for the spiral in the domain II. In the doped film at H = 62 mT, t = 100 nm, Eq. 2, gives an amplitude suppression $A \approx 0.13$, and in the t = 141 nm doped film, $A \approx 0.16$. These numbers are consistent with the Lorentz microscopy experimental data, where the suppression of the amplitude of the spiral in domain II is A ~ 0.1 to 0.2.

Last, on the basis of a series of temperature dependent measurements, the H-T phase diagrams for the both doped and undoped samples are shown in Fig. 6. Figure 6 (A to D) represents measurements on the Te-doped sample, whereas Fig. 6 (E to H) was obtained on the undoped sample. The colored regions in both cases denote the appearance of the skyrmion phase. Thickness dependences are clearly seen for both samples; the stable H-T space of SkLs increased with decreasing film thickness. In addition, the skyrmion phase diagrams are quantitatively different for the Te-doped CSO compared to the undoped CSO. For example, the critical magnetic fields (dashed lines on phase diagrams in Fig. 6) to nucleate/annihilate skyrmions in the temperature range of 20 to 40 K are larger for the Te-doped CSO compared to those of undoped CSO. We note that the SkL stability is more strongly dependent on sample thickness compared to that for the undoped sample. In addition, when the film thickness is above 100 nm, a slight tendency of skyrmion phase splitting is observed (see Fig. 6, C and D for t = 141 and 174 nm) for the doped sample, which is consistent with the recently reported two independent skyrmion phases (*35*) and the skyrmion phase splitting reported for Zn-doped CSO crystals (*47*). This indicates that the Te doping promotes the separation between the thermal fluctuation–induced skyrmion phase at high temperature and the second skyrmion phase at low temperature. Thus, the Te doping in CSO crystals provides an advantageous platform to investigate the second skyrmion phase in thin films. Previously, chemical doping was reported to stabilize the metastable skyrmion phases at low temperature. We note that there are differences in our obtained phase diagrams compared to chemical doping effects in bulk crystals studied by neutron scattering studies (*11*, *48*, *49*), which highlight the importance of boundary conditions and the thin-film geometry on the evolution of skyrmion phases.

In summary, the dynamics of the helical and skyrmion phases in thin films of multiferroic Te-doped and undoped CSO with discrete thickness sections are investigated systematically using in situ Lorentz microscopy. We find that, with increasing applied field, the helical-to-skyrmion phase transition are characterized by anisotropic scaling of spiral helical-phase periodicities, from edge-enhanced skyrmion nucleation to gradual skyrmion channeling to thicker sections. Our

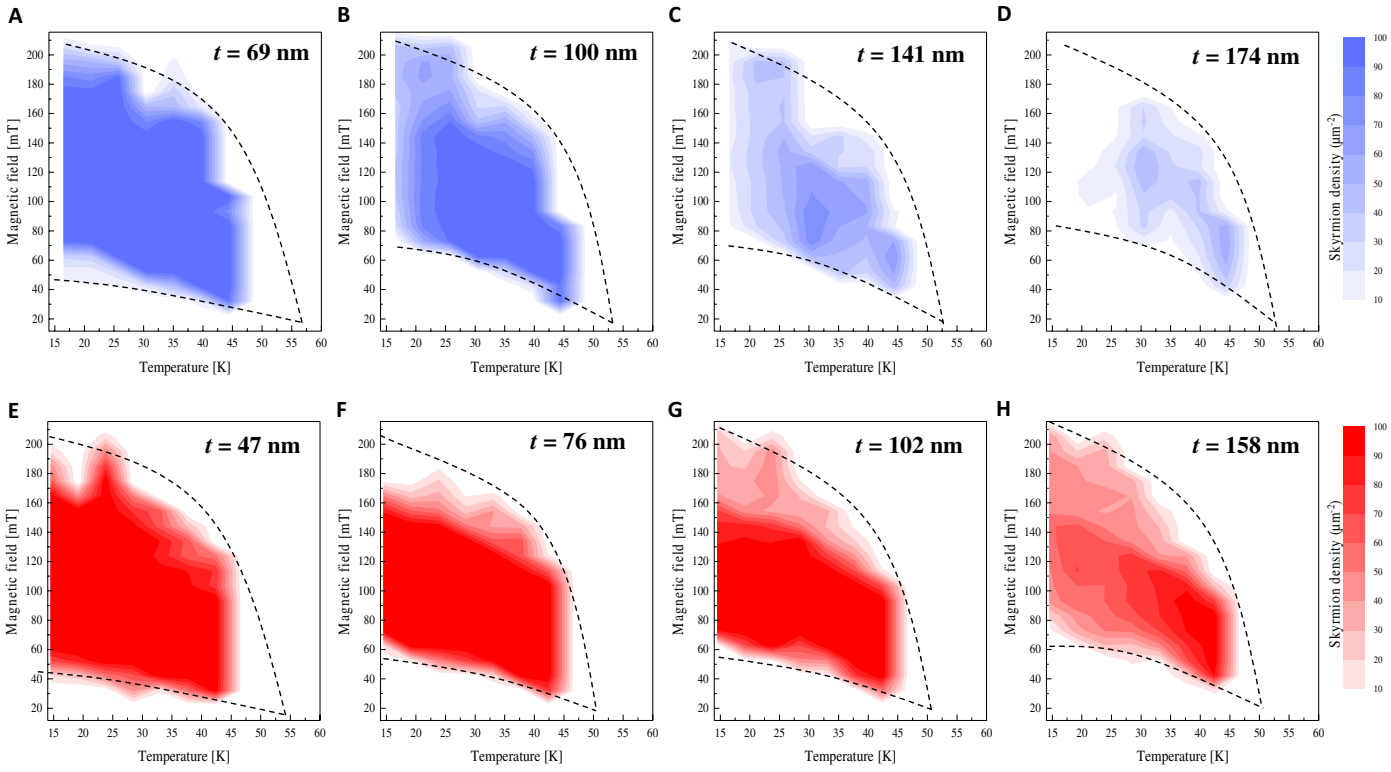

Fig. 6. Phase diagrams as function of doping and thickness. Magnetic field–temperature phase maps of the both doped (**A** to **D**) and undoped (**E** to **H**) CSO crystals with increasing film thickness, respectively. The doped sample shows the SkL stability is more strongly dependent on film thickness compared to the undoped sample. Both doped and undoped samples show that SkLs are more stable with decreasing film thickness.

theoretical study shows that the anisotropic scaling behavior of helices is the result of out-of-plane tilting of the helix. Thickness-dependent gradual skyrmion channeling and enhanced dependence on boundary conditions by Te doping reported in this study shed new light on the SkL manipulation for skyrmion-based spintronics.

MATERIALS AND METHODS

Single-crystalline undoped and Te-doped CSO crystals were synthesized by the chemical vapor transport method (*19*) yielding millimeter-sized crystals. Detailed information on synthesis and crystal characterization can be found in the Supplementary Materials. To investigate the effects of chemical doping and sample thickness on the skyrmion phase dynamics, transmission electron microscopy (TEM) samples with various thicknesses were prepared by FIB. Schematics of TEM samples and Lorentz images of undoped and Te-doped samples are shown in Fig. 1 (A to C). Each undoped and Te-doped CSO samples have four sections of different thickness, which are measured by the low-loss function of electron energy-loss spectroscopy. The thin films prepared in [$\bar{1}$10] orientation have thicknesses in the range between 50 and 200 nm, as shown in Fig. 1. The mean free path for inelastic scattering for both Te-doped and undoped samples are estimated as 88.62 and 85.89 nm, respectively, by the averaged atomic mass using a method given by Egerton (*50*). Because of FIB-induced damages on both top and bottom surfaces of TEM sample (*51*), the thicknesses estimated by low-loss spectra can be overestimated by ~10 nm. An aberration-corrected JEOL ARM 200CF microscope at Brookhaven National Laboratory was used for Lorentz phase imaging performed along the [$\bar{1}$10] direction. The out-of-the plane magnetic field in the electron microscope has been calibrated using a custom-made Hall probe TEM holder, as previously reported (*17*, *52*). The TEM samples are cooled with a customized liquid-helium cooling holder (HCHDT3010, Gatan UK Inc.) down to 12 K.

SUPPLEMENTARY MATERIALS

Supplementary material for this article is available at http://advances.sciencemag.org/cgi/content/full/6/13/eaax2138/DC1

X-ray diffraction
Energy-dispersive x-ray spectroscopy
Second skyrmion phase at lower T and higher magnetic field
Micromagnetic simulation
Theoretical analysis
Table S1. Crystal data and structure refinement for $Cu_2OSe(Te)O_3$.
Table S2. Fractional atomic coordinates and equivalent isotropic displacement parameters ($Å^2 \times 10^3$).
Table 3. Anisotropic displacement parameters ($Å^2 \times 10^3$).
Fig. S1. Energy-dispersive x-ray spectroscopy maps of Cu, Se, O, and Te.
Fig. S2. Skyrmion phase diagrams obtained from Te-doped and undoped TEM samples with relatively uniform thickness (~150 nm).
Fig. S3. Micromagnetic simulations.
Movie S1. Video of Te-doped sample under increasing magnetic field at 15 K.
Movie S2. Video of Te-doped sample under increasing magnetic field at 25 K.
Movie S3. Video of Te-doped sample under increasing magnetic field at 40 K.
Movie S4. Video of undoped sample under increasing magnetic field at 15 K.
Movie S5. Video of undoped sample under increasing magnetic field at 25 K.
Movie S6. Video of undoped sample under increasing magnetic field at 40 K.
References (*53*, *54*)

REFERENCES AND NOTES

1. T. H. R. Skyrme, A unified field theory of mesons and baryons. *Nucl. Phys.* **31**, 556–569 (1962).
2. K. Everschor, Thesis, Universität zu Köln (2012).

3. A. Fert, V. Cros, J. Sampaio, Skyrmions on the track. *Nat. Nanotechnol.* **8**, 152–156 (2013).
4. S. S. P. Parkin, M. Hayashi, L. Thomas, Magnetic domain-wall racetrack memory. *Science* **320**, 190–194 (2008).
5. R. Wiesendanger, Nanoscale magnetic skyrmions in metallic films and multilayers: A new twist for spintronics. *Nat. Rev. Mater.* **1**, 16044 (2016).
6. C. Pfleiderer, A. Rosch, Condensed-matter physics: Single skyrmions spotted. *Nature* **465**, 880–881 (2010).
7. U. K. Rößler, A. N. Bogdanov, C. Pfleiderer, Spontaneous skyrmion ground states in magnetic metals. *Nature* **442**, 797–801 (2006).
8. A. Bogdanov, A. Hubert, Thermodynamically stable magnetic vortex states in magnetic crystals. *J. Magn. Magn. Mater.* **138**, 255–269 (1994).
9. A. N. Bogdanov, D. A. Yablonskiĭ, Thermodynamically stable" vortices" in magnetically ordered crystals. The mixed state of magnets. *Zh. Eksp. Teor. Fiz* **95**, 178–182 (1989).
10. S. Mühlbauer, B. Binz, F. Jonietz, C. Pfleiderer, A. Rosch, A. Neubauer, R. Georgii, P. Böni, Skyrmion lattice in a chiral magnet. *Science* **323**, 915–919 (2009).
11. W. Münzer, A. Neubauer, T. Adams, S. Mühlbauer, C. Franz, F. Jonietz, R. Georgii, P. Böni, B. Pedersen, M. Schmidt, A. Rosch, C. Pfleiderer, Skyrmion lattice in the doped semiconductor Fe_{1-x} Co_xSi. *Phys. Rev. B* **81**, 041203 (2010).
12. X. Z. Yu, Y. Onose, N. Kanazawa, J. H. Park, J. H. Han, Y. Matsui, N. Nagaosa, Y. Tokura, Real-space observation of a two-dimensional skyrmion crystal. *Nature* **465**, 901–904 (2010).
13. P. Milde, D. Köhler, J. Seidel, L. M. Eng, A. Bauer, A. Chacon, J. Kindervater, S. Mühlbauer, C. Pfleiderer, S. Buhrandt, C. Schütte, A. Rosch, Unwinding of a skyrmion lattice by magnetic monopoles. *Science* **340**, 1076–1080 (2013).
14. Y. Tokunaga, X. Z. Yu, J. S. White, H. M. Rønnow, D. Morikawa, Y. Taguchi, Y. Tokura, A new class of chiral materials hosting magnetic skyrmions beyond room temperature. *Nat. Commun.* **6**, 7638 (2015).
15. C. Moreau-Luchaire, C. Moutafis, N. Reyren, J. Sampaio, C. A. F. Vaz, N. Van Horne, K. Bouzehouane, K. Garcia, C. Deranlot, P. Warnicke, P. Wohlhüter, J.-M. George, M. Weigand, J. Raabe, V. Cros, A. Fert, Additive interfacial chiral interaction in multilayers for stabilization of small individual skyrmions at room temperature. *Nat. Nanotechnol.* **11**, 444–448 (2016).
16. S. Woo, K. Litzius, B. Krüger, M.-Y. Im, L. Caretta, K. Richter, M. Mann, A. Krone, R. M. Reeve, M. Weigand, P. Agrawal, I. Lemesh, M.-A. Mawass, P. Fischer, M. Kläui, G. S. D. Beach, Observation of room-temperature magnetic skyrmions and their current-driven dynamics in ultrathin metallic ferromagnets. *Nat. Mater.* **15**, 501–506 (2016).
17. S. D. Pollard, J. A. Garlow, J. Yu, Z. Wang, Y. Zhu, H. Yang, Observation of stable néel skyrmions in cobalt/palladium multilayers with Lorentz transmission electron microscopy. *Nat. Commun.* **8**, 14761 (2017).
18. J. A. Garlow, S. D. Pollard, M. Beleggia, T. Dutta, H. Yang, Y. Zhu, Quantification of mixed Bloch-Néel topological spin textures stabilized by the Dzyaloshinskii-Moriya interaction in Co / Pd multilayers. *Phys. Rev. Lett.* **122**, 237201 (2019).
19. S. Seki, X. Z. Yu, S. Ishiwata, Y. Tokura, Observation of skyrmions in a multiferroic material. *Science* **336**, 198–201 (2012).
20. E. Ruff, S. Widmann, P. Lunkenheimer, V. Tsurkan, S. Bordács, I. Kézsmárki, A. Loidl, Multiferroicity and skyrmions carrying electric polarization in GaV_4S_8. *Sci. Adv.* **1**, e1500916 (2015).
21. R. Tomasello, E. Martinez, R. Zivieri, L. Torres, M. Carpentieri, G. Finocchio, A strategy for the design of skyrmion racetrack memories. *Sci. Rep.* **4**, 6784 (2014).
22. M.-C. Chen, K. Roy, Magnetic Skyrmions for Cache Memory. arXiv:1705.01095, (2017).
23. M. Schott, A. Bernand-Mantel, L. Ranno, S. Pizzini, J. Vogel, H. Béa, C. Baraduc, S. Auffret, G. Gaudin, D. Givord, The skyrmion switch: Turning magnetic skyrmion bubbles on and off with an electric field. *Nano Lett.* **17**, 3006–3012 (2017).
24. D. Pinna, F. Abreu Araujo, J.-V. Kim, V. Cros, D. Querlioz, P. Bessiere, J. Droulez, J. Grollier, Skyrmion gas manipulation for probabilistic computing. *Phys. Rev. Applied* **9**, 064018 (2018).
25. A. Fert, N. Reyren, V. Cros, Magnetic skyrmions: Advances in physics and potential applications. *Nat. Rev. Mater.* **2**, 17031 (2017).
26. G. Finocchio, F. Büttner, R. Tomasello, M. Carpentieri, M. Kläui, Magnetic skyrmions: From fundamental to applications. *J. Phys. D Appl. Phys.* **49**, 423001 (2016).
27. F. Jonietz, S. Mühlbauer, C. Pfleiderer, A. Neubauer, W. Münzer, A. Bauer, T. Adams, R. Georgii, P. Böni, R. A. Duine, K. Everschor, M. Garst, A. Rosch, Spin transfer torques in MnSi at ultralow current densities. *Science* **330**, 1648–1651 (2010).
28. P.-J. Hsu, A. Kubetzka, A. Finco, N. Romming, K. von Bergmann, R. Wiesendanger, Electric-field-driven switching of individual magnetic skyrmions. *Nat. Nanotechnol.* **12**, 123–126 (2017).
29. Y. Nii, T. Nakajima, A. Kikkawa, Y. Yamasaki, K. Ohishi, J. Suzuki, Y. Taguchi, T. Arima, Y. Tokura, Y. Iwasa, Uniaxial stress control of skyrmion phase. *Nat. Commun.* **6**, 8539 (2015).
30. X. Z. Yu, N. Kanazawa, W. Z. Zhang, T. Nagai, T. Hara, K. Kimoto, Y. Matsui, Y. Onose, Y. Tokura, Skyrmion flow near room temperature in an ultralow current density. *Nat. Commun.* **3**, 988 (2012).
31. H. S. Park, X. Yu, S. Aizawa, T. Tanigaki, T. Akashi, Y. Takahashi, T. Matsuda, N. Kanazawa, Y. Onose, D. Shindo, A. Tonomura, Y. Tokura, Observation of the magnetic flux and three-dimensional structure of skyrmion lattices by electron holography. *Nat. Nanotechnol.* **9**, 337–342 (2014).
32. M. Mochizuki, Creation of skyrmions by electric field on chiral-lattice magnetic insulators. *Adv. Electron. Mater.* **2**, 1500180 (2016).
33. A. Rosch, Spintronics: Electric control of skyrmions. *Nat. Nanotechnol.* **12**, 103–104 (2016).
34. D. Bhattacharya, M. M. Al-Rashid, J. Atulasimha, Voltage controlled core reversal of fixed magnetic skyrmions without a magnetic field. *Sci. Rep.* **6**, 31272 (2016).
35. F. Qian, L. J. Bannenberg, H. Wilhelm, G. Chaboussant, L. M. Debeer-Schmitt, M. P. Schmidt, A. Aqeel, T. T. M. Palstra, E. Brück, A. J. E. Lefering, C. Pappas, M. Mostovoy, A. O. Leonov, New magnetic phase of the chiral skyrmion material Cu_2OSeO_3. *Sci. Adv.* **4**, eaat7323 (2018).
36. A. Chacon, L. Heinen, M. Halder, A. Bauer, W. Simeth, S. Mühlbauer, H. Berger, M. Garst, A. Rosch, C. Pfleiderer, Observation of two independent skyrmion phases in a chiral magnetic material. *Nat. Phys.* **14**, 936–941 (2018).
37. L. J. Bannenberg, H. Wilhelm, R. Cubitt, A. Labh, M. P. Schmidt, E. Lelièvre-Berna, C. Pappas, M. Mostovoy, A. O. Leonov, Multiple low-temperature skyrmionic states in a bulk chiral magnet. *npj Quantum Mater.* **4**, 11 (2019).
38. N. Kanazawa, S. Seki, Y. Tokura, Noncentrosymmetric magnets hosting magnetic skyrmions. *Adv. Mater.* **29**, 1603227 (2017).
39. A. Karatay, B. Küçüköz, G. Çankaya, A. Ates, A. Elmali, The effect of Se/Te ratio on transient absorption behavior and nonlinear absorption properties of $CuIn_{0.7}Ga_{0.3}(Se_{1-x}Te_x)_2$ ($0 \leq x \leq 1$) amorphous semiconductor thin films. *Opt. Mater.* **73**, 20–24 (2017).
40. M. Beleggia, M. A. Schofield, V. V. Volkov, Y. Zhu, On the transport of intensity technique for phase retrieval. *Ultramicroscopy* **102**, 37–49 (2004).
41. K. Shibata, X. Z. Yu, T. Hara, D. Morikawa, N. Kanazawa, K. Kimoto, S. Ishiwata, Y. Matsui, Y. Tokura, Towards control of the size and helicity of skyrmions in helimagnetic alloys by spin–Orbit coupling. *Nat. Nanotechnol.* **8**, 723–728 (2013).
42. H. Du, R. Che, L. Kong, X. Zhao, C. Jin, C. Wang, J. Yang, W. Ning, R. Li, C. Jin, X. Chen, J. Zang, Y. Zhang, M. Tian, Edge-mediated skyrmion chain and its collective dynamics in a confined geometry. *Nat. Commun.* **6**, 8504 (2015).
43. C. Jin, Z.-A. Li, A. Kovács, J. Caron, F. Zheng, F. N. Rybakov, N. S. Kiselev, H. Du, S. Blügel, M. Tian, Y. Zhang, M. Farle, R. E. Dunin-Borkowski, Control of morphology and formation of highly geometrically confined magnetic skyrmions. *Nat. Commun.* **8**, 15569 (2017).
44. A. O. Leonov, M. Mostovoy, Edge states and skyrmion dynamics in nanostripes of frustrated magnets. *Nat. Commun.* **8**, 14394 (2017).
45. J. Müller, A. Rosch, M. Garst, Edge instabilities and skyrmion creation in magnetic layers. *New J. Phys.* **18**, 065006 (2016).
46. S. Seki, Y. Okamura, K. Kondou, K. Shibata, M. Kubota, R. Takagi, F. Kagawa, M. Kawasaki, G. Tatara, Y. Otani, Y. Tokura, Magnetochiral nonreciprocity of volume spin wave propagation in chiral-lattice ferromagnets. *Phys. Rev. B* **93**, 235131 (2016).
47. H. C. Wu, T. Y. Wei, K. D. Chandrasekhar, T. Y. Chen, H. Berger, H. D. Yang, Unexpected observation of splitting of skyrmion phase in Zn doped Cu_2OSeO_3. *Sci. Rep.* **5**, 13579 (2015).
48. M. T. Birch, R. Takagi, S. Seki, M. N. Wilson, F. Kagawa, A. Štefančič, G. Balakrishnan, R. Fan, P. Steadman, C. J. Ottley, M. Crisanti, R. Cubitt, T. Lancaster, Y. Tokura, P. D. Hatton, Increased lifetime of metastable skyrmions by controlled doping. *Phys. Rev. B* **100**, 014425 (2019).
49. L. J. Bannenberg, K. Kakurai, F. Qian, E. Lelièvre-Berna, C. D. Dewhurst, Y. Onose, Y. Endoh, Y. Tokura, C. Pappas, Extended skyrmion lattice scattering and long-time memory in the chiral magnet Fe_{1-x} Co_x Si. *Phys. Rev. B* **94**, 104406 (2016).
50. R. F. Egerton, *Electron Energy-Loss Spectroscopy in the Electron Microscope* (Springer Science & Business Media, 2011).
51. Z. Wang, T. Kato, T. Hirayama, N. Kato, K. Sasaki, H. Saka, Surface damage induced by focused-ion-beam milling in a Si/Si p–n junction cross-sectional specimen. *Appl. Surf. Sci.* **241**, 80–86 (2005).
52. J. W. Lau, M. A. Schofield, Y. Zhu, A straightforward specimen holder modification for remnant magnetic-field measurement in TEM. *Ultramicroscopy* **107**, 396–400 (2007).
53. O. V. Dolomanov, L. J. Bourhis, R. J. Gildea, J. A. K. Howard, H. Puschmann, *OLEX2*: A complete structure solution, refinement and analysis program. *J. Appl. Cryst.* **42**, 339–341 (2009).
54. G. M. Sheldrick, Crystal structure refinement with SHELXL. *Acta Crystallogr. C Struct. Chem.* **71**, 3–8 (2015).

Acknowledgments

Funding: The work at Brookhaven National Laboratory is supported by the Materials Science and Engineering Divisions, Office of Basic Energy Sciences of the U.S. Department of Energy under contract no. DESC0012704. TEM sample preparation was performed at the Center for Functional Nanomaterials, Brookhaven National Laboratory. We acknowledge support by the Australian Research Council through Discovery Grants. **Author contributions:** M.-G.H., C.U.,

T.S., and J.Se. contrived the idea for the experimental work. M.-G.H. and J.A.G. performed TEM measurements and analyses under the guidance of Y.Z. K.K. and T.K. assisted TEM sample preparation. L.C., R.R., and T.S. synthesized and characterized materials. Y.K. and O.S. performed theoretical calculations. J.Se., M.-G.H., Y.K., G.V., and Y.Z. analyzed data and co-wrote the manuscript with input from all authors. All authors discussed and contributed to the writing of the manuscript. **Competing interests:** The authors declare that they have no competing interests. **Data and materials availability:** All data needed to evaluate the conclusions in the paper are present in the paper and/or the Supplementary Materials. Additional data related to this paper may be requested from the authors.

Submitted 4 March 2019
Accepted 3 January 2020
Published 27 March 2020
10.1126/sciadv.aax2138

Citation: M.-G. Han, J. A. Garlow, Y. Kharkov, L. Camacho, R. Rov, J. Sauceda, G. Vats, K. Kisslinger, T. Kato, O. Sushkov, Y. Zhu, C. Ulrich, T. Söhnel, J. Seidel, Scaling, rotation, and channeling behavior of helical and skyrmion spin textures in thin films of Te-doped Cu_2OSeO_3. *Sci. Adv.* **6**, eaax2138 (2020).